

# ARIES: Cylindrical Pendulum Actuated Explorer Sphere

Bruno Belzile, *Member, IEEE* and David St-Onge, *Member, IEEE*

**Abstract**—Spherical rolling robots (SRR) have been a promising avenue for the exploration of unstructured environments with variable topologies. The advantages include the ability to move fast, robustness to collision and a lower number of actuators. However, to finally be used in real missions and applications, they need to have a high maneuverability and have sufficient inner space to house a proper payload for the intended application, such as cave and tunnel exploration, without compromising on the performances. With barycentric spherical robot, adding mass with a payload may become challenging, as the location of the center-of-mass (CoM) is critical for the locomotion. In this paper, we propose a novel barycentric spherical robot with two degrees-of-freedom (DoF) named Autonomous Robotic Intelligent Explorer Spheres (ARIES). The motion of this SRR is generated by a cylindrical actuated joint acting like a 2-DoF pendulum. This design allows us to have a nearly empty upper hemisphere inside the spherical shell, which is dedicated to payloads adapted to the application. The full kinematics and dynamics are presented, and simulation results are included. The control scheme implemented is detailed. We conducted an experimental evaluation of the ARIES with different trajectories, as well as discussed practical considerations and future improvements.

**Index Terms**—Mobile robot, kinematics, dynamics, control.

## I. INTRODUCTION

THE modes of locomotion of mobile robots on the ground can typically be classified in three main categories: 1) wheeled, 2) legged or 3) spherical. Ideally, a robot locomotion system should be designed for a given set of tasks and terrain topology. On the one hand, wheeled robots can generate high velocities and accelerations, but they are not so good when they encounter obstacles [1]. Indeed, with only one point of contact on the ground, a spherical robot easily maneuver around an obstacle, or even use the latter to orient itself. On the other hand, spherical rolling robots (SRR) are more stable than legged robots on unstructured terrains with various topologies and are also particularly appropriate for harsh environments, as the critical inner parts such as the electronics are protected by an other shell [1]. In fact, this attribute makes SSRs particularly interesting for underground and planetary exploration [2], [3]. A wide range of inner mechanisms have been developed for SRR actuation by many researchers, each with its own advantages and disadvantages [4].

Extending previous work [5] with more theoretical and experimental content, we propose in this paper a spherical rolling robot actuated by a differential cylindrical drive named



Fig. 1. Autonomous Robotic Intelligent Explorer Sphere (ARIES)

ARIES<sup>1</sup>, standing for Autonomous Robotic Intelligent Explorer Spheres. Contrary to most barycentric spherical robots, which use the displacement of their center-of-mass (CoM) to generate the motion, our robot does not use rotations as degrees-of-freedom (DoF) inside the spherical shell, but a cylindrical motion of the CoM. The implementation of an actuated cylindrical joint makes it possible to use two identical motors, as well as freeing the upper hemisphere of the robot for a payload, such as instruments for simultaneous localization and mapping (SLAM). As we previously shown [5], the cylindrical pendulum has several advantages compared to a more conventional 2-DoF tilting pendulum, notably with respect to the curvature radius. Compared to the paper where we initially presented the concept of the cylindrical-pendulum-driven SRR, we developed here a full model of the kinematics and dynamics of the system, rather than simplified (decoupled) models which are often found in the literature [1]. Moreover, we also included the heading kinematics, which were validated experimentally with an inertial measurement unit (IMU) and encoders. As further additional content, the control scheme used on the prototype is presented. In the sequel, a review of the relevant literature on similar spherical rolling robot designs is first done in Section II. The concept and modeling of the pendulum-based barycentric spherical robot are then detailed in Section III. Our implementation of the actuated cylindrical pendulum is then presented in Section IV, followed by the complete prototype in Section V. Experimental data acquired during various tests is finally presented and discussed in Section VI.

B. Belzile and D. St-Onge are with the Department of Mechanical Engineering, École de technologie supérieure, Montréal, Canada, e-mail: bruno.belzile.1@ens.etsmtl.ca

Manuscript received January 20, 2022; revised April 4, 2022.

<sup>1</sup>patent pending

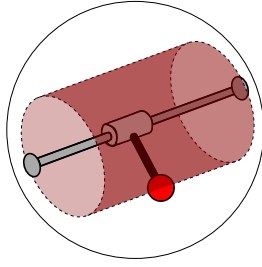


Fig. 2. Cylindrical surface representing the feasible locations of the CoM (illustrated by a smaller red sphere), which is rigidly attached to a link (of negligible mass) to a cylindrical joint on the central axis of the spherical shell

## II. RELEVANT WORK

A large range of spherical rolling robots can be found in the literature for various applications, ranging from child-development studies [6] to agriculture [7]. Some are also commercially available, commonly sold as toys to learn robotics [8]. While there are as many spherical rolling robot designs as there are specific sets of characteristics, their locomotion systems can be summarized in three broad categories: 1) barycentric [9], [10]; 2) conservation of the angular momentum [11], [12]; and 3) shell deformation [13], [14]. In this paper, only barycentric spherical robots are considered, as opposed to those based on the conservation of the angular momentum and shell deformation, as well as spherical robots using outer forces, such as the NASA/JPL Tumbleweed polar rover [15], those with external limbs [16] and those meant for underwater applications [17].

By far the most common type of spherical robots [4], barycentric spherical robots (BSR) are driven by a displacement of their center of mass (CoM). Indeed, destabilizing the system by moving the CoM away from its point of lowest potential energy (typically directly underneath the center of rotation (CoR) of the sphere) allows the shell to start rolling. The BSRs can be classified in several subcategories: 1) pendulum-based; 2) internal drive unit (IDU); 3) sliding masses.

First, in a pendulum-based BSRs, the pendulum bob points in the direction of desired travel; these are fairly common. The pendulum typically, but not necessarily, rotates about a shaft passing through the center of the sphere. While only one bob is needed, Li, Deng and Liu proposed a BSR with two [18] and DeJong et al., four [10] to increase their maneuverability, at the expense of more complex control schemes. Moreover, multiple pendulums do not need to be fully independent from each other. Asiri et al. [1] added a second, smaller, pendulum orthogonal to the main pendulum rotating about their spherical shell's main axis. Otherwise, to steer its single-pendulum BSR, Schroll [19] designed and patented a differential mechanism to tilt the bob in a direction orthogonal to the rolling motion.

Second, some researchers have also built prototypes with a smaller wheeled robot inside the sphere [20] or with an internal drive unit (IDU) [21]. However, these systems are known to suffer from slipping between the internal drive and the spherical shell [4], limiting their robustness. Finally, some BSRs use sliding masses to control the location of the CoM [22], [23]. They are generally more difficult to control

than the two other subcategories described above.

## III. BARYCENTRIC SPHERICAL ROBOT WITH A CYLINDRICAL PENDULUM

As mentioned above, the proposed barycentric spherical robot rolls on the ground with a motion induced by a displacement of the center-of-mass, which is done by an actuated pendulum. To be able to steer the sphere as well, and not only roll forward and backward in one single direction, two controlled DoFs are required. In the design we propose, the CoM can be displaced over a cylinder inside the sphere, as shown in Fig. 2. If the cylindrical joint is not located at the center of the sphere, i.e. it underwent a translation from its original position, the ARIES will tilt on one side, as illustrated in Fig. 3. Then, with a simple rotation of the pendulum about the axis of the cylindrical joint, the robot will roll and steer at the same time. Because of the nature of the cylindrical joint, namely independent translation and rotation, the steering angle can be changed as it rolls. The cylindrical actuated joint is therefore a differential transmission. Our implementation of an actuated cylindrical joint, visible in Fig. 3, is presented in Section IV, but first, to derive the SRR model, we will use the simplified representation of Fig. 2.

### A. Mobility

The Chebychev-Grübler-Kutzbach (CGK) formula [24] confirms that this cylindrical actuated joint mechanism has two DoFs, namely,

$$f = d(l - 1) - \sum_{i=1}^p r_i = 2(4 - 1) - 4 \times 1 = 2 \quad (1)$$

where  $d$ ,  $l$ ,  $p$  and  $r_i$  are respectively the dimension of the simplest subgroup containing all the Lie subgroups of the joints involved, the number of links, the number of kinematic pairs (joints) and the degree of constraint of each joint.

### B. Kinematics

This section presents the equations relating the translational and angular displacement of the cylindrical drive to the spherical motion. Five frames are required for this derivation:

- 1) the inertial reference frame  $\mathcal{F}$ ;
- 2) the frame  $\mathcal{F}_o$  that is rotated by the angle  $\psi$  about the  $z$ -axis of  $\mathcal{F}$ ;
- 3) the moving reference frame  $\mathcal{F}_m$  attached to the center of the sphere, only allowed to translate with respect to  $\mathcal{F}_o$ ;
- 4) the frame attached to the center of the shell  $\mathcal{F}_s$ , with its  $x$ -axis aligned with the main rotation axis of the mechanism;
- 5) the frame attached to the CoM of the pendulum  $\mathcal{F}_p$ , which is obtained after applying a translation  $u$  and a rotation  $\alpha$  about the  $x$ -axis of  $\mathcal{F}_s$  (axis of the cylindrical joint).

All five frames are illustrated in Fig. 4. The orientation of the ARIES, namely the angles defining  $\mathcal{F}_s$  with respect to  $\mathcal{F}$ , can be computed with the three Euler angles  $\psi$ ,  $\theta$  and  $\phi$  using the following sequence of rotations: 1) a rotation  $\psi$  about the  $z$ -axis of  $\mathcal{F}$ , resulting in frame  $\mathcal{F}_m$ ; 2) a rotation

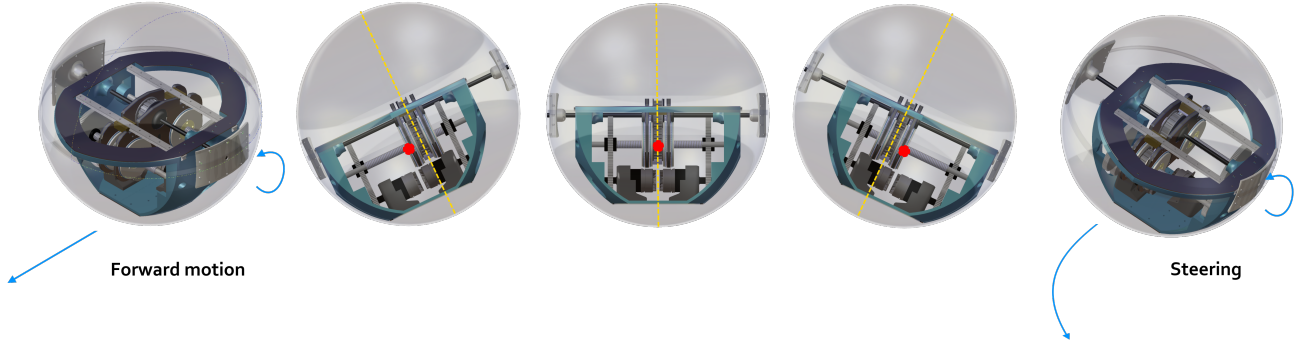


Fig. 3. Locomotion with a cylindrical pendulum; the CoM (red dot) is moved away from the central plane (yellow dashed line) to steer the robot; if the CoM is on the central plane, a rotation of the pendulum shaft will generate a forward/backward motion

$\theta$  about the  $x$ -axis of  $\mathcal{F}_m$ , resulting in the intermediate frame  $\mathcal{F}'$ ; 3) a rotation  $\phi$  about the  $y$ -axis of  $\mathcal{F}'$ , resulting in the frame  $\mathcal{F}_s$ . The resulting  $(4 \times 4)$  homogeneous transformation matrix defining the orientation and position of the ARIES in the reference frame  $\mathcal{F}$  is thus

$$\mathbf{H}_s = \mathbf{H}_o(x, y) \mathbf{H}_Z(\psi) \mathbf{H}_X(\theta) \mathbf{H}_Y(\phi) \quad (2a)$$

with

$$\mathbf{H}_o(x_s, y_s) = \begin{bmatrix} \mathbf{R}_o & d_s \\ \mathbf{0}^T & 1 \end{bmatrix} = \begin{bmatrix} 1 & 0 & 0 & x_s \\ 0 & 1 & 0 & y_s \\ 0 & 0 & 1 & 0 \\ 0 & 0 & 0 & 1 \end{bmatrix} \quad (2b)$$

$$\mathbf{H}_Z(\psi) = \begin{bmatrix} \mathbf{R}_Z & \mathbf{0} \\ \mathbf{0}^T & 1 \end{bmatrix} = \begin{bmatrix} \cos \psi & -\sin \psi & 0 & 0 \\ \sin \psi & \cos \psi & 0 & 0 \\ 0 & 0 & 1 & 0 \\ 0 & 0 & 0 & 1 \end{bmatrix} \quad (2c)$$

$$\mathbf{H}_X(\theta) = \begin{bmatrix} \mathbf{R}_X & \mathbf{0} \\ \mathbf{0}^T & 1 \end{bmatrix} = \begin{bmatrix} 1 & 0 & 0 & 0 \\ 0 & \cos \theta & -\sin \theta & 0 \\ 0 & \sin \theta & \cos \theta & 0 \\ 0 & 0 & 0 & 1 \end{bmatrix} \quad (2d)$$

$$\mathbf{H}_Y(\phi) = \begin{bmatrix} \mathbf{R}_Y & \mathbf{0} \\ \mathbf{0}^T & 1 \end{bmatrix} = \begin{bmatrix} \cos \phi & 0 & \sin \phi & 0 \\ 0 & 1 & 0 & 0 \\ -\sin \phi & 0 & \cos \phi & 0 \\ 0 & 0 & 0 & 1 \end{bmatrix} \quad (2e)$$

where  $(x_s, y_s)$  are the coordinates of the origin of frame  $\mathcal{F}_m$  in  $\mathcal{F}$  and  $\mathbf{R}_i$  is the rotation submatrix of  $\mathbf{H}_i$ . A gimbal lock is in theory possible with this Euler angle convention, but it is not problematic since the system only has two DoFs, and in the end it is the position of the CoM or of the robot that is controlled, not the orientation. In the following, the left superscript of a variable refers to its frame, e.g.  ${}^s \mathbf{r}_p$  in  $\mathcal{F}_s$ . On the one hand, the Cartesian position of the center of the sphere with respect to the reference frame  $\mathcal{F}$  is  $\mathbf{p}_s = [x_s \ y_s \ R]^T$ , where  $R$  is the radius of the shell. On the other hand, the position of the CoM of the cylindrical pendulum with respect to frame  $\mathcal{F}_s$  is

$${}^s \mathbf{r}_p = [u \ r \sin \alpha \ -r \cos \alpha]^T \quad (3)$$

where  $r$  is the distance between the axis of the cylindrical joint passing through the center of the sphere and the CoM of the pendulum. Variables  $u$  and  $\alpha$  are, respectively, the translational

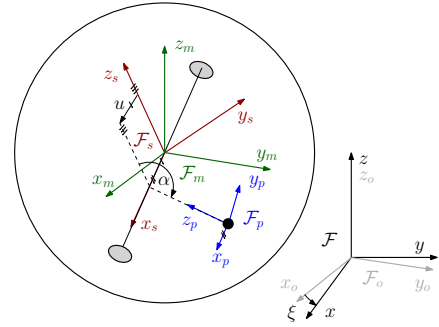


Fig. 4. Frames:  $\mathcal{F}$  and  $\mathcal{F}_o$  attached to the ground,  $\mathcal{F}_m$  and  $\mathcal{F}_s$  attached to the center of the sphere,  $\mathcal{F}_p$  attached to the CoM of the pendulum

and rotational output of the cylindrical joint. The homogeneous transformation matrix representing the orientation and translation of the cylindrical pendulum in  $\mathcal{F}_s$  is therefore

$${}^s \mathbf{H}_p = \begin{bmatrix} 1 & 0 & 0 & u \\ 0 & \cos \phi & -\sin \phi & r \sin \alpha \\ 0 & \sin \phi & \cos \phi & -r \cos \alpha \\ 0 & 0 & 0 & 1 \end{bmatrix} \quad (4)$$

The homogeneous transformation matrix representing the orientation and position of the CoM of the cylindrical pendulum is thus, in  $\mathcal{F}$ ,

$$\mathbf{H}_p = \mathbf{H}_s {}^s \mathbf{H}_p \quad (5)$$

The angular velocity of the sphere in  $\mathcal{F}_s$  is computed with the following expression:

$${}^s \boldsymbol{\omega}_s = \begin{bmatrix} \dot{\theta} \cos \phi - \dot{\psi} \cos \theta \sin \phi \\ \dot{\phi} + \dot{\psi} \sin \theta \\ \dot{\psi} \cos \theta \cos \phi + \dot{\theta} \sin \phi \end{bmatrix} \quad (6)$$

Similarly, the expression of the angular velocity of the pendulum in frame  $\mathcal{F}_p$  is obtained, i.e.

$${}^p \boldsymbol{\omega}_p = [\dot{\alpha} \ 0 \ 0]^T \quad (7)$$

Using the  $(3 \times 3)$  rotation submatrix of the homogeneous transformation matrix given in (4) and expression (6), the pendulum's angular velocity in frame  $\mathcal{F}_s$  is defined as

$${}^s \boldsymbol{\omega}_p = {}^s \mathbf{R}_p {}^p \boldsymbol{\omega}_p + {}^s \boldsymbol{\omega}_s \quad (8)$$

Finally, we must consider the kinematics related to the non-slipping condition. Indeed, this creates a constraint between the angular and linear velocities of the spherical shell. First, we define the angular velocity in frame  $\mathcal{F}$ , i.e.

$$\boldsymbol{\omega}_s = \mathbf{R}_Z(\psi)\mathbf{R}_X(\theta)\mathbf{R}_Y(\phi) {}^s\boldsymbol{\omega}_s = \mathbf{R}_s {}^s\boldsymbol{\omega}_s \quad (9)$$

Therefore, we have the two following constraint equations, which are non-holonomic (preventing skidding and rotating on itself without rolling on the ground):

$$C_1 = \dot{x}_s - R\omega_{s,y} = 0, \quad C_2 = \dot{y}_s + R\omega_{s,x} = 0 \quad (10)$$

The non-slipping assumption has obviously some limitations. While internal slipping is not an issue with a pendulum-driven system, external slipping between the ground and the shell can still happen under some circumstances, including high torque and granular soil. Continuous slipping can significantly limit the maneuverability of any spherical robot, while momentary slipping can affect localization based on some sensors such as encoders. The location of the CoM with respect to the mass of the system is therefore crucial to minimize the risk.

### C. Heading

Assuming that the orientation of the pendulum in frame  $\mathcal{F}$  is known, for instance with an IMU, the heading of the robot can be computed with the inverse kinematics. Indeed, only considering the orientation part of eq. (5), we have

$$\mathbf{R}_s = \mathbf{R}_p {}^s\mathbf{R}_p^T \quad (11)$$

where  $\mathbf{R}_p$  and  ${}^s\mathbf{R}_p$  are known with the measurements of the IMU and the position sensors in cylindrical joint (to be determined later), respectively. Moreover, the angular velocity vector of the sphere in frame  $\mathcal{F}_s$ , namely (6), being easily computed from the angular velocities measured in frame  $\mathcal{F}_p$  and the angular velocity of the cylindrical joint, we can thus compute  $\boldsymbol{\omega}_s$  from (9) with eq. (11). With the constraint equations defined in (10), we can finally compute the heading of the robot, i.e.

$$\zeta = \text{atan2}(\dot{y}_s, \dot{x}_s) = \text{atan2}(-\omega_{s,x}, \omega_{s,y}) \quad (12)$$

This expression can be computed in real time with the sensors mentioned above.

### D. Dynamics

With the kinematics of the robot, we can now derive its dynamics model. Similar to other spherical rolling robots, the equations of motion of the ARIES are highly nonlinear [11]. First, some common assumptions are required to formulate the dynamics model with a pendulum:

- 1) at static equilibrium, the pendulum is in a vertical downward position and is located at the center of the main rotating axis, i.e. the  $z$ -axis of  $\mathcal{F}_p$  passes through the origin of  $\mathcal{F}_s$  and is parallel to the  $z$ -axis of  $\mathcal{F}$ ;
- 2) the system is rolling, without slipping, over a perfectly horizontal surface;

- 3) the internal dynamics of the actuated cylindrical joint (which is presented in Section IV) can be neglected with respect to the resulting forces and torques.

Concerning the second assumption, it is not a requirement, but a hypothesis to simplify the dynamic equations derived in this paper, as we do not consider other external forces applied on the system than the reaction from the ground. This model, however, can be generalized to consider obstacles and uneven terrains. We recall the reference frames depicted in Fig. 4 for this analysis. The Lagrangian approach is chosen to obtain the equations of motion. First, a set of generalized coordinates  $\{q_i\}$  representing the location and orientation of the sphere and the cylindrical pendulum must be defined, i.e.

$$\mathbf{q} = [\psi \quad \theta \quad \phi \quad x_s \quad y_s \quad \alpha \quad u]^T \quad (13)$$

where the first three are the Euler angles of the shell, the following two are the coordinates of the robot on the ground and the last two are the rotation and translation of the cylindrical joint, respectively. The generalized coordinates defined, the expressions of the kinetic energy are then computed with

$$K_s = \frac{1}{2} (m_s \dot{\mathbf{p}}_s^T \dot{\mathbf{p}}_s + {}^s\boldsymbol{\omega}_s^T \mathbf{I}_s {}^s\boldsymbol{\omega}_s) \quad (14a)$$

$$K_p = \frac{1}{2} (m_p \dot{\mathbf{p}}_p^T \dot{\mathbf{p}}_p + {}^s\boldsymbol{\omega}_p^T \mathbf{I}_p {}^s\boldsymbol{\omega}_p) \quad (14b)$$

where  $m_s$ ,  $\mathbf{I}_s$ ,  $m_p$  and  $\mathbf{I}_p$  are, respectively, the mass and inertia tensors of the shell and pendulum. With the CoM of the shell located at the geometrical center of the sphere and only flat surfaces considered as mentioned above, the expression of the potential energy is, with the gravitational acceleration  $g$ ,

$$E_p = m_p g p_{p,z} \quad (15)$$

From  $K_s$ ,  $K_p$  and  $E_p$  a Lagrangian function is obtained:

$$L = K_s + K_p - E_p \quad (16)$$

The Euler-Lagrange equations are therefore

$$\frac{d}{dt} \left( \frac{\partial L}{\partial \dot{q}_i} \right) - \frac{\partial L}{\partial q_i} = \tau_i + \boldsymbol{\lambda}^T \mathbf{a}_i \quad (17)$$

where  $\tau_i$  is the generalized force associated with the generalized coordinate  $q_i$ . Obviously, the generalized coordinates are not all independent. Therefore, the two non-slipping constraint equations defined earlier are integrated in the Euler-Lagrange equations with the Lagrange multipliers  $\boldsymbol{\lambda} = [\lambda_1 \quad \lambda_2]$  and the 2-dimensional vectors  $\mathbf{a}_i$  defined as

$$[\mathbf{a}_1 \quad \mathbf{a}_2 \quad \dots \quad \mathbf{a}_7] = \begin{bmatrix} \partial C_1 / \partial \dot{\mathbf{q}} \\ \partial C_2 / \partial \dot{\mathbf{q}} \end{bmatrix} \quad (18)$$

The generalized forces  $\tau_6$  and  $\tau_7$  are, respectively, equal to  $\tau$  and  $f$ , the torque and force output of the cylindrical joint. Therefore, we have 9 unknowns, namely 7 generalized coordinates defined in (13) and 2 Lagrangian multipliers  $\lambda_i$ , as well as 9 equations, i.e. eqs. (10) and (17).

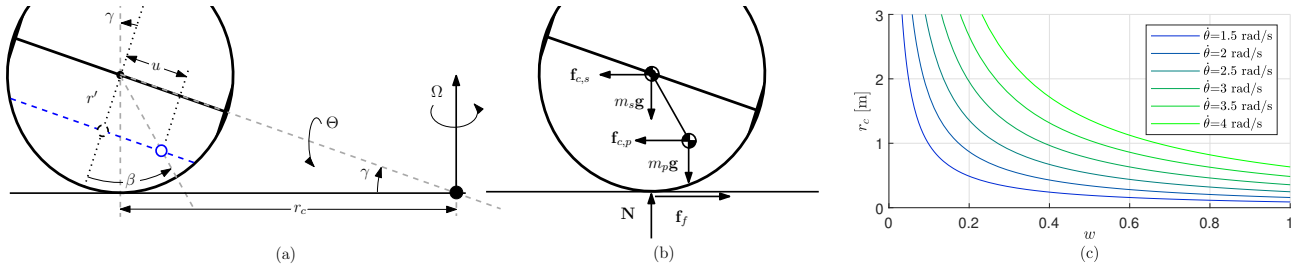


Fig. 5. Steering motion: (a) geometrical model; (b) lateral forces and moments; (c) curvature radius

### E. Curvature Radius

The next essential element to consider is the curvature radius while the ARIES steers, as shown in Fig. 5 where the geometrical parameters and variables are defined. To this aim, a similar approach to the one used by Kayacan et al. [25] and Asiri et al. [1] is applied here. The same simplifications and variables are used here to make the comparison easier, instead of using exactly the model described in the previous section. Regardless of the steering mechanism chosen, the angular velocity of the spherical robot about the vertical axis of the reference frame  $\mathcal{F}$  is

$$\dot{\psi} = -R\dot{\Theta}/r_c \quad (19)$$

where  $R$ ,  $\dot{\Theta}$  and  $r_c$  are, respectively, the radius of the sphere, the rolling angular velocity of the sphere (which should not be confused with  $\dot{\theta}$  defined earlier; depending on the orientation of the sphere, they can be equal) and the radius of curvature while steering. Therefore, since none of the first two are affected by the steering mechanism, tilting and cylindrical mechanisms must be compared over how the radius of curvature  $r_c$  is generated. It should be noted that variables used to define the state of the BSR are slightly different than those presented in Section III-B in order to simplify the equations. For the cylindrical pendulum, the magnitude of the friction force between the ground and the sphere is computed with the following expression:

$$\begin{aligned} \|\mathbf{f}_f\| &= \|\mathbf{f}_{c,s}\| + \|\mathbf{f}_{c,p}\| \\ &= m_s r_c \dot{\psi}^2 + m_p (r_c + u \cos \gamma) \dot{\psi}^2 \\ &\approx (m_s + m_p) r_c \dot{\psi}^2 \end{aligned} \quad (20)$$

where  $\mathbf{f}_{c,i}$ ,  $i = \{s, p\}$  are the centrifugal forces acting on the sphere and the pendulum and  $\dot{\psi}$  is the angular velocity of the sphere about the  $z$ -axis in  $\mathcal{F}$ . As can be seen, the translation component of the cylindrical pendulum is neglected, as  $r_c$  is assumed significantly larger than  $u$ . Then, the magnitude of the torque acting about the transversal axis of the sphere, i.e. the  $y$ -axis of frame  $\mathcal{F}_s$ , is computed with

$$\begin{aligned} T_y &= -R\|\mathbf{f}_f\| - m_p g (r' \sin \gamma + u \cos \gamma) \\ &\quad + \|\mathbf{f}_{c,p}\| (r' \cos \gamma - u \sin \gamma) \\ &\approx -R(m_s + m_p) r_c \dot{\psi}^2 - m_p g (r' \sin \gamma + u \cos \gamma) \\ &\quad + m_p r_c \dot{\psi}^2 (r' \cos \gamma - u \sin \gamma) \end{aligned} \quad (21)$$

Knowing that the angular velocity of the sphere, in  $\mathcal{F}_m$ , is

$${}^m \boldsymbol{\omega}_s = [-\dot{\Theta} \cos \gamma \quad -\dot{\gamma} \quad \dot{\psi} - \dot{\Theta} \sin \gamma]^T \quad (22)$$

and that its angular momentum is defined as (the planar moment of inertia of the shell is assumed to be the same regardless of the plane, i.e.  $r I_s = t I_s = I_s$ )

$$\mathbf{L} = I_s \boldsymbol{\omega} = [-I_s \dot{\Theta} \cos \gamma \quad -I_s \dot{\gamma} \quad I_s (\dot{\psi} - \dot{\Theta} \sin \gamma)]^T \quad (23)$$

then the total torque applied on the sphere, which is the time derivative of  $\mathbf{L}$ , can also be obtained as  $\mathbf{T} = \boldsymbol{\Omega} \times \mathbf{L}$  since the sphere is undergoing uniform circular motion<sup>2</sup>, i.e.

$$\mathbf{T} = [I_s \dot{\psi} \dot{\gamma} \quad -I_s \dot{\psi} \dot{\Theta} \cos \gamma \quad 0]^T \quad (24)$$

Therefore, the second component of  $\mathbf{T}$  (from eq. (24)) must be equal to  $T_y$  (from eq. (21)). After some simplifications and using a small-angle assumption for  $\gamma$ , we have

$$r_c \approx \frac{-m_p r' R^2 \dot{\Theta}^2 + I_s R \dot{\Theta}^2 + R^3 (m_s + m_p) \dot{\Theta}^2}{u m_p g} \quad (25)$$

The resulting curvature radius for different rolling velocities and normalized tilting angles was computed and is shown in Fig. 5(c). The normalized tilting angle is defined as  $w = \beta/30^\circ$ , where  $30^\circ$  is the expected maximum value of  $\beta$  (realistic maximum value with regards to the scale of our prototype discussed in the next section and other devices found in the literature). The numerical values of the parameters used to generate these curves are included in Table I, and we assumed  $r = r'$ .

TABLE I  
PARAMETERS USED FOR THE CURVATURE RADIUS COMPUTATION

$I_s$	$I_p$	$m_s$	$m_p$	$R$	$r$	$g$
0.25 kgm <sup>2</sup>	0.2 kgm <sup>2</sup>	1 kg	5 kg	0.2 m	0.1 m	9.81 $\frac{m}{s^2}$

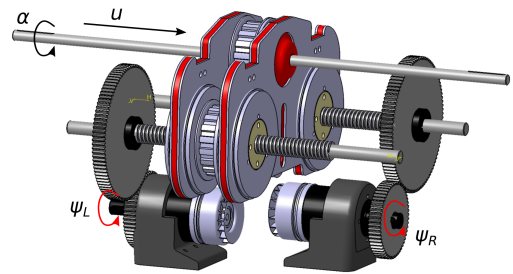


Fig. 6. Rendering of the cylindrical pendulum only, casing enveloping the pendulum not shown (the motors are rigidly attached to the casing)

<sup>2</sup>Here,  $\boldsymbol{\Omega}$  is the angular velocity vector defining the uniform circular motion, i.e.  $\boldsymbol{\Omega} = [0 \quad 0 \quad \dot{\psi}]^T$  and should not be confused with  $\boldsymbol{\omega}$ .

#### IV. CYLINDRICAL DRIVE ACTUATION

A cylindrical drive is a differential mechanism with two DoFs, a rotation and a translation, about the same axis (in our case passing through the center of the sphere). Harada et al. designed one example of this kind of mechanisms, dubbed the C-drive, with a RHHR<sup>3</sup> kinematic chain [26]. Karimi, Eskandary and Angeles later improved the device with belts and pulleys shaped into a translating  $\Pi$ -joint [27] that was used to drive a two-limb isostatic pick-and-place robot [28].

Inspired by this work, our design, shown in Fig. 6, transforms the concept into a novel implementation. In both applications, two identical revolute motors are used to reduce the complexity and two lead screws with the same pitch, one righthand, the other lefthand, support the linear motion. In their implementation, Karimi Eskandary and Angeles attached the motors of the C-drive to the base and the output shaft was connected to the first link of a manipulator. Instead, in our approach the motors are rigidly attached to the mobile platform (pendulum), as shown in Fig. 3. The motors of our cylindrical drive are moving inside the spherical shell by translating about the rolling axis of the robot, as depicted in Fig. 3. The output of this cylindrical drive generates the rotation required for the sphere to roll plus the translation needed for it to steer. Therefore, the mechanism was fundamentally rethink for this different output as well as to minimize its mass; an important criterion for mobile robots mostly absent from industrial manipulator design.

##### A. Kinematics

As mentioned above, the pulleys can only rotate about their axis, therefore cannot translate inside the sphere, as depicted in Fig. 3. Array  $\mathbf{d}$ , the output of the cylindrical joint, is mapped by the  $(2 \times 2)$  Jacobian matrix  $\mathbf{J}$  into the joint variables  $\psi$ :

$$\psi = \mathbf{J}\mathbf{d}, \quad \mathbf{J} \equiv \frac{1}{p} \begin{bmatrix} 2\pi & pG \\ -2\pi & pG \end{bmatrix}, \quad \mathbf{d} = [u \quad \alpha]^T \quad (26)$$

where  $u$  and  $\alpha$ , as mentioned above, are the translational and rotational output of the cylindrical joint,  $G$  and  $p$  are, respectively, the gear-reduction ratio of the mechanism and the pitch of the lead screws (the same for symmetry).

The resulting Jacobian matrix in eq. (26) is constant and of full rank; useful features for control. Finally, it should be noted that the transpose of the Jacobian matrix can be used to compute the generalized forces  $\tau$  and  $f$  previously mentioned with the following equation:

$$\begin{bmatrix} f \\ \tau \end{bmatrix} = \mathbf{J}^T \begin{bmatrix} \tau_L \\ \tau_R \end{bmatrix} \quad (27)$$

##### B. Prototype of the cylindrical pendulum

The cylindrical pendulum is illustrated in Fig. 6. The two revolute actuators, Maxon EC 45 flat 30 W brushless motors (26:1 reduction ratio), are rigidly attached to the casing of the pendulum. They were selected for their mass and to fit in

<sup>3</sup>R, H and C stand for revolute, helical (screw) and cylindrical joint respectively.

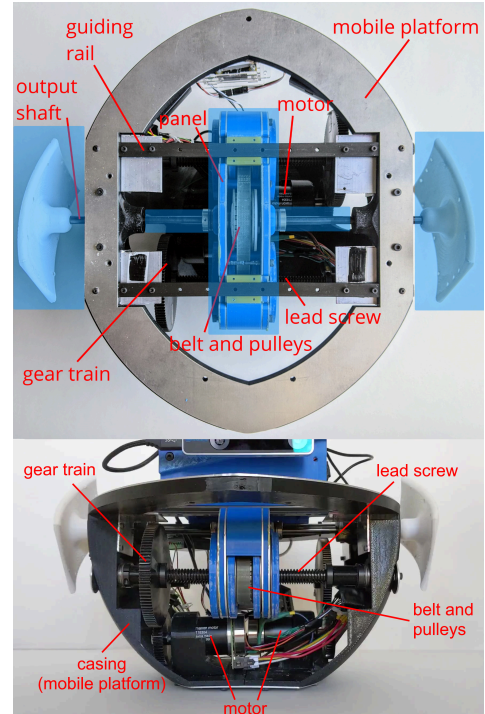


Fig. 7. Above view (all parts that can translate relative to the mobile platform are highlighted in blue) and front view of the cylindrical drive (payload platform visible on top)

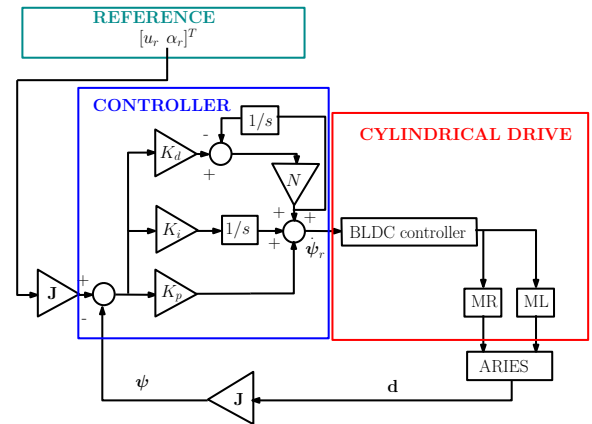


Fig. 8. Control scheme (ML: left motor; MR: right motor)

the limited available space. Maxon controllers for brushless DC (BLDC) motors were also chosen. Gears are used to lower the CoM by putting the motors parallel and underneath the lead screws. This increases the translation range of the mechanism. Pulleys are coupled to the nuts. Thrust bearings and two side panels (aluminum-ABS-aluminum to increase rigidity to weight ratio) are used to assure that the pulleys remain in the same plane. The upper pulley is rigidly attached to the rolling axis of the robot. Two guiding rails, parallel two the screws and the main shaft, are included. Thereby, the pulleys are not translating inside the sphere, they only rotate, as can be seen in Fig. 7. It is the inner mechanism casing that translates (not shown in Fig. 6) in order to tilt the shell. Some structural parts were 3D printed to complete the mechanism.

### C. Control

The control scheme is programmed in Python within the Robot Operating System (ROS) environment. The ARIES has two independent control variables: the rotation and the translation of the pendulum, corresponding, respectively, to the rolling and the steering motion of the sphere. Moreover, remember that  $u$  is approximately proportional to the inverse of the curvature radius  $r_c$ , as demonstrated in an earlier paper [5]. To control these two variables, we implemented a PID position controller<sup>4</sup>, which is illustrated in Fig. 8. As mentioned above, the angular position of the motor actuating the cylindrical pendulum, namely  $\psi$ , is measured with optical encoders and to obtain accurate heading of the robot while rolling, an inertial measurement unit (IMU) rigidly attached to the pendulum is used to compute its orientation. The measurements from the IMU are processed by the Madgwick filter [29], which returns the quaternions defining the orientation. The feedback from the sensors can be visualized remotely over wifi, but the control happens onboard. The reference is obtained from remote controller communicating over Bluetooth directly with the ARIES, but a script trajectory could also be implemented and published through ROS. The remote controller node in ROS publishes linear and angular velocities, which are applied to the cylindrical pendulum, not the sphere.

## V. PROTOTYPE OF THE ARIES

A prototype of the ARIES was built to experimentally test its capabilities and is depicted in Fig. 1. The cylindrical drive, which was already presented in Section IV, is meant to be encompassed inside a polycarbonate transparent shell divided into two hemispheres, with an overlapping section to guarantee hermeticity and an adequate curvature. It can be seen in Fig. 1.

The system is controlled by an on-board Nvidia Jetson Xavier NX. For prototyping purposes, Phidget modules are used to generate the necessary inputs/outputs: directions and references for the motors, feedback from the quadrature encoders, etc. The Phidget modules communicate with the Xavier NX through two USB ports. For data acquisition and the experiments presented in Section VI, two current sensors are included to measure the total current passing through each motor. The ARIES was designed in the first place for applications involving SLAM. Therefore, it is equipped with a 3D LiDAR, the Blickfeld Cube1, and two Intel Realsense cameras (D435i and T265) in addition to the on-board electronics previously mentioned. Considering the large space available in the upper hemisphere of the robot, the payload can easily be modified to follow the mission needs.

## VI. EXPERIMENTS AND DISCUSSION

Several experiments were conducted to validate the capabilities of the ARIES, focusing on three elements, i.e. the rotation of the cylindrical pendulum/rolling, its translation/steering and the rolling with a steering angle. First, The curvature radius was determined experimentally to validate the concept of the actuated cylindrical pendulum and the model of the system. As

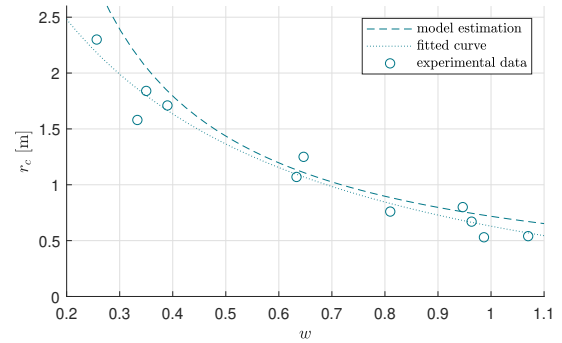


Fig. 9. Experimental curvature radius for  $\dot{\theta} = 4.26$  rad/s; dashed curves for estimation from the model, circles for experimental data

shown in Fig. 9, the experimental data approach the curvature estimated by the model for the tested velocity. The noticeable discrepancies can be explained by friction in the mechanism, assumptions made in the model and inertial parameters that do not perfectly fit reality. Nevertheless, this shows that the ARIES can be steered with a relatively small curvature radius at a reasonable speed and be controlled.

Second, the current at each motor, filtered to remove high frequency noise, was measured during a simple forward trajectory without any steering. The resulting trajectory, with the position obtained from the odometry of the T265, is illustrated in Fig. 10(a). The result shows a minor deviation of less than 5% without close-loop position control nor the operator's intervention. The other measurements are shown in Fig. 10(b-c). As expected, angle  $\phi$  remains close to zero for a forward motion on a flat surface. Two other meaningful angles are displayed in the righthand side of this figure. As can be seen, the ARIES rolled at a constant desired forward velocity generated by the rotation of the pendulum, i.e.  $\alpha$ . The pendulum was pointing downward for most of this trajectory, as illustrated by the  $\epsilon$ , which is the roll angle obtained by the IMU attached to the pendulum. The fact that  $\alpha$  and  $\gamma$  closely follow each other at the beginning of the motion is explained by the torque necessary to start the motion, which is not zero. On the lefthand side of the same figure, the current in the motors is displayed. Because the CoM position is controlled and not the torque, there are discrepancies between both motors. Friction and compliance in the cylindrical mechanism explain most of these differences. Previous robot designs actuated with cylindrical drives, such as the PMC mentioned earlier, show similar variation of the torque in experiments, even with ballscrews to reduce friction on a rigid mechanism made of aluminum [27].

We also validate the performance with measurements obtained during a translation of the cylindrical pendulum (from left to right) while the ARIES remains stationary, i.e. without rolling, see Fig. 11. Again, the current in the motors and the pitch angle of the pendulum/sphere ( $\phi$ ) were measured. As the figure shows, because of friction, no current is needed to keep an arbitrary tilting angle (visible at the beginning). Moreover, the discrepancies between the two motors are also caused by the internal friction of the mechanism. A continuous variation of the tilting angle was obtained, as shown in

<sup>4</sup>Parameters of the PID:  $K_p = 0.02$ ,  $K_d = 0.0004$ ,  $K_i = 0$

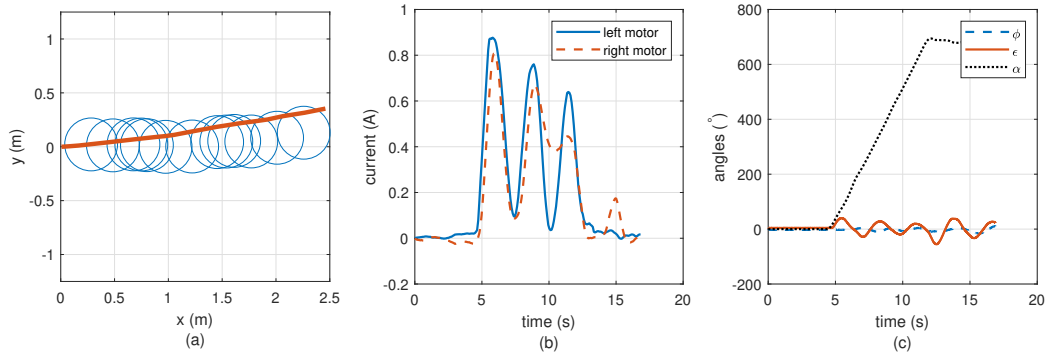


Fig. 10. Forward rolling of the ARIES: (a) trajectory obtained from visual odometry (blue circles) and estimated from IMU and encoders (red curve); (b) current measured in the motors; (c) orientation of the pendulum and rotation of the cylindrical joint

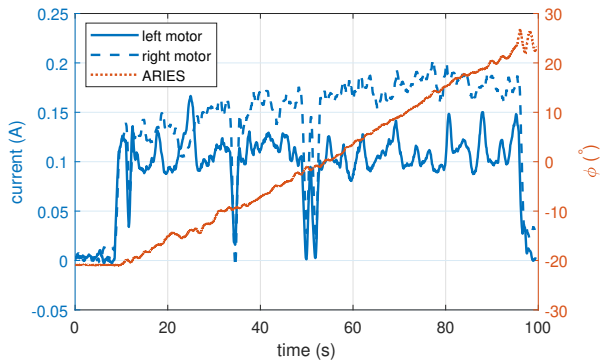


Fig. 11. Tilting of the ARIES induced by a translation of the cylindrical pendulum

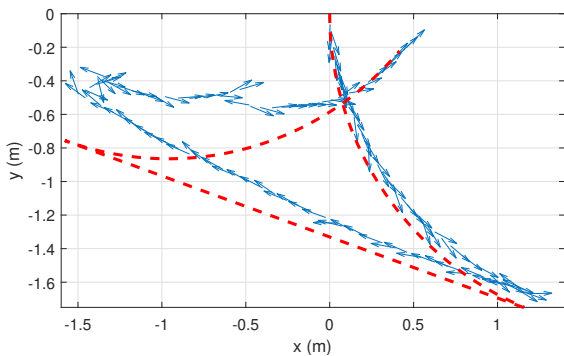


Fig. 12. Complex trajectory starting at  $(0, 0)$ , with heading shown by arrows and desired trajectory by the dashed curve

the same figure. Considering the internal friction mentioned above, future improvements will include an optimization of the mechanism to reduce its effect, for example using ballscrews instead of lead screws, as well as a qualitative comparison with other SRRs.

Finally, to complete the experimental validation, we ran a more complex trajectory, including steering as well as forward and backward motions, to assess the maneuverability of the system, with multiple changes of direction. As shown in Fig. 12, it includes first a curved path, followed by a backward motion in straight line and another curve mirroring the beginning of the trajectory. The dashed curve is the desired path, showing relatively minor deviation obtained without close-loop position control. Arrows in this figure depict the heading computed online with the equations of Section III-C. Indeed,

${}^s\mathbf{R}_p$  is obtained from the encoders, and  ${}^s\mathbf{R}_p$  is computed from the IMU measurements, which is attached to the pendulum. We can therefore solve eq. (11). Locations where the heading arrows displayed seem more erratic correspond to moments when the ARIES actuators are no longer generating torque to drive the sphere. In these situations, after the motion is stopped, the residual kinetic energy is dissipated by small oscillations caused by the spherical nature of the robot.

## VII. CONCLUSION

In this paper, a novel barycentric SRR driven by a cylindrical pendulum was presented. This 2-DoF differential mechanism allows simultaneous rolling and steering with a robust mechanism actuated by only two identical motors. Kinematics and dynamics of the system were first presented, followed by the implementation of the cylindrical joint. The modeling shows that simple input/output equations can be used to control the robot. Therefore, a PID control scheme was implemented to control the location of the CoM to generate both the rolling and steering motions. A full prototype was finally presented, with several experiments. Future work will include optimal control of this spherical robot and its integration into a swarm of heterogeneous robots for exploration.

## ACKNOWLEDGMENT

This work was supported by NSERC Discovery Grant (RGPIN-2020-06121) and the Canadian Space Agency (CSA-FAST 19FAPOLA32).

## REFERENCES

- [1] S. Asiri, F. Khademianzadeh, A. Monadjemi, and P. Moallem, "The Design and Development of a Dynamic Model of a Low-Power Consumption, Two-Pendulum Spherical Robot," *IEEE/ASME Transactions on Mechatronics*, vol. 24, no. 5, pp. 2406–2415, 2019.
- [2] F. R. Hogan and J. R. Forbes, "Modeling of spherical robots rolling on generic surfaces," *Multibody System Dynamics*, vol. 35, no. 1, pp. 91–109, 2015.
- [3] J. Ocampo-Jiménez, A. Muñoz-Meléndez, and G. Rodríguez-Gómez, "Extending a spherical robot for dealing with irregular surfaces: a sea urchin-like robot," *Advanced Robotics*, vol. 28, no. 22, pp. 1475–1485, 2014.
- [4] R. Chase and A. Pandya, "A Review of Active Mechanical Driving Principles of Spherical Robots," *Robotics*, vol. 1, no. 1, pp. 3–23, 2012.
- [5] B. Belzile and D. St-Onge, "Design and Modeling of a Spherical Robot Actuated by a Cylindrical Drive," *IEEE International Conference on Robotics and Automation (ICRA)*, 2022.

- [6] F. Michaud, J. F. Laplante, H. Larouche, A. Duquette, S. Caron, D. Létourneau, and P. Masson, "Autonomous spherical mobile robot for child-development studies," *IEEE Transactions on Systems, Man, and Cybernetics Part A: Systems and Humans*, vol. 35, no. 4, pp. 471–480, 2005.
- [7] J. D. Hernández, J. Barrientos, J. Del Cerro, A. Barrientos, and D. Sanz, "Moisture measurement in crops using spherical robots," *Industrial Robot*, vol. 40, no. 1, pp. 59–66, 2013.
- [8] A. Wheeler, S. Smith, and D. Gardner, "Using the Sphero BOLT to Engage Students Mathematically," *Journal of Mathematics Education at Teachers College*, vol. 11, no. 2, pp. 55–60, 2020.
- [9] K. Landa and A. K. Pilat, "Design and start-up of spherical robot with internal pendulum," in *10th International Workshop on Robot Motion and Control*. IEEE, 2015, pp. 27–32.
- [10] B. P. DeJong, E. Karadogan, K. Yelamarthi, and J. Hasbany, "Design and Analysis of a Four-Pendulum Omnidirectional Spherical Robot," *J Intell Robot Syst*, vol. 86, pp. 3–15, 2017.
- [11] G. C. Schroll, "Dynamic Model of a Spherical Robot from First Principles," Ph.D. dissertation, 2010.
- [12] J. Chen, P. Ye, H. Sun, and Q. Jia, "Design and motion control of a spherical robot with control moment gyroscope," in *2016 3rd International Conference on Systems and Informatics*. IEEE, 2017, pp. 114–120.
- [13] K. W. Wait, P. J. Jackson, and L. S. Smoot, "Self locomotion of a spherical rolling robot using a novel deformable pneumatic method," in *Proceedings of the IEEE International Conference on Robotics and Automation*, 2010, pp. 3757–3762.
- [14] Y. shan Liang, X. li Zhang, H. Huang, Y. feng Yang, W. tao Jin, and Z. xun Sang, "A deformable spherical planet exploration robot," in *International Conference on Graphic and Image Processing (ICGIP 2012)*, vol. 8768, International Society for Optics and Photonics. SPIE, 2013, inproceedings, pp. 57 – 63.
- [15] A. Behar, F. Carsey, J. Matthews, and J. Jones, "NASA/JPL tumbleweed polar rover," in *IEEE Aerospace Conference Proceedings*, vol. 1, 2004, pp. 388–395.
- [16] H. Xing, L. Shi, X. Hou, Y. Liu, Y. Hu, D. Xia, Z. Li, and S. Guo, "Design, modeling and control of a miniature bio-inspired amphibious spherical robot," *Mechatronics*, vol. 77, p. 102574, 2021.
- [17] R. Eldred, J. Lussier, and A. Pollman, "Design and testing of a spherical autonomous underwater vehicle for shipwreck interior exploration," *Journal of Marine Science and Engineering*, vol. 9, no. 3, p. 320, 2021.
- [18] B. Li, Q. Deng, and Z. Liu, "A spherical hopping robot for exploration in complex environments," in *2009 IEEE International Conference on Robotics and Biomimetics, ROBIO 2009*, 2009, pp. 402–407.
- [19] G. C. Schroll, "Angular momentum torque enhancement for spherical vehicles," 2009.
- [20] J. Alves and J. Dias, "Design and control of a spherical mobile robot," *Proc. of the Institution of Mechanical Engineers, Part I: Journal of Systems and Control Engineering*, vol. 217, no. 6, pp. 457–467, 2003.
- [21] A. Bicchi, A. Balluchi, D. Prattichizzo, and A. Gorelli, "Introducing the 'SPHERICLE': An experimental testbed for research and teaching in nonholonomy," in *IEEE International Conference on Robotics and Automation*, vol. 3. IEEE, 1997, pp. 2620–2625.
- [22] A. H. A. Javadi and P. Mojabi, "Introducing August: A novel strategy for an omnidirectional spherical rolling robot," *IEEE International Conference on Robotics and Automation*, vol. 4, pp. 3527–3533, 2002.
- [23] J. Bowkett, M. Burkhardt, and J. W. Burdick, "Combined Energy Harvesting and Control of Moball: A Barycentric Spherical Robot," in *ISER 2016: 2016 International Symposium on Experimental Robotics*. Springer, Cham, 2017, pp. 71–83.
- [24] J. M. Hervé, "The Lie group of rigid body displacements, a fundamental tool for mechanism design," *Mechanism and Machine theory*, vol. 34, no. 5, pp. 719–730, 1999.
- [25] E. Kayacan, Z. Y. Bayraktaroglu, and W. Saeys, "Modeling and control of a spherical rolling robot: A decoupled dynamics approach," *Robotica*, vol. 30, no. 4, pp. 671–680, 2012.
- [26] T. Harada, T. Friedlaender, and J. Angeles, "The development of an innovative two-DOF cylindrical drive: Design, analysis and preliminary tests," in *IEEE International Conference on Robotics and Automation*. IEEE, 2014, pp. 6338–6344.
- [27] P. Karimi Eskandary and J. Angeles, "The translating II-joint: Design and applications," *Mechanism and Machine Theory*, vol. 122, pp. 361–370, 2018.
- [28] B. Belzile, P. Karimi Eskandary, and J. Angeles, "Workspace Determination and Feedback Control of a Pick-and-Place Parallel Robot: Analysis and Experiments," *IEEE Robotics and Automation Letters*, vol. 5, no. 1, pp. 40–47, 2020.
- [29] S. Madgwick, "An efficient orientation filter for inertial and inertial/magnetic sensor arrays," *Report x-io and University of Bristol (UK)*, vol. 25, pp. 113–118, 2010.



**Bruno Belzile** (Member, IEEE) is a research associate at the École de technologie supérieure. He holds a B.Eng. degree and Ph.D. in mechanical engineering from Polytechnique Montréal. His thesis focused on underactuated grippers and proprioceptive tactile sensing. He continued his research in robotics at the Center for Intelligent Machines at McGill University, where he worked on kinematics, dynamics and control of parallel robots. He was the recipient of the FRQNT Étudiant-chercheur étoile Award in 2017 and the Best Research Paper Award

in robotics and mechatronics at the IFToMM World Congress in 2019.



**David St-Onge** (Member, IEEE) is an Associate Professor with the Mechanical Engineering Department, at the École de technologie supérieure in Montreal since 2019, where he is the director of the INIT Robots Lab. He holds a M.Sc. and Ph.D. degrees in mechanical engineering from Université Laval, Canada. He has over ten years experience in the field of interactive media (structure, automatization and sensing) as workshop production director and as a research and development engineer. He is a certified UAV pilot and flight evaluator. He participates in

the UTILI CREATE program, training HQP for drone services, as well as the CoRoM CREATE program, training HQP for the deployment of industrial robots. His research focuses on robotic swarms' control through expressive motions (human/robots) and cognitive ergonomics in robot teams' operation.

## LIST OF FIGURES

1	Autonomous Robotic Intelligent Explorer Sphere (ARIES) . . . . .	1
2	Cylindrical surface representing the feasible locations of the CoM (illustrated by a smaller red sphere), which is rigidly attached to a link (of negligible mass) to a cylindrical joint on the central axis of the spherical shell . . .	2
3	Locomotion with a cylindrical pendulum; the CoM (red dot) is moved away from the central plane (yellow dashed line) to steer the robot; if the CoM is on the central plane, a rotation of the pendulum shaft will generate a forward/backward motion . . . . .	3
4	Frames: $\mathcal{F}$ and $\mathcal{F}_o$ attached to the ground, $\mathcal{F}_m$ and $\mathcal{F}_s$ attached to the center of the sphere, $\mathcal{F}_p$ attached to the CoM of the pendulum . . . . .	3
5	Steering motion: (a) geometrical model; (b) lateral forces and moments; (c) curvature radius . . . . .	5
6	Rendering of the cylindrical pendulum only, casing enveloping the pendulum not shown (the motors are rigidly attached to the casing) . . . . .	5
7	Above view (all parts that can translate relative to the mobile platform are highlighted in blue) and front view of the cylindrical drive (payload platform visible on top) . . . . .	6
8	Control scheme (ML: left motor; MR: right motor) . . . . .	6
9	Experimental curvature radius for $\dot{\theta} = 4.26$ rad/s; dashed curves for estimation from the model, circles for experimental data . . . . .	7
10	Forward rolling of the ARIES: (a) trajectory obtained from visual odometry (blue circles) and estimated from IMU and encoders (red curve); (b) current measured in the motors; (c) orientation of the pendulum and rotation of the cylindrical joint . . . . .	8
11	Tilting of the ARIES induced by a translation of the cylindrical pendulum . . . . .	8
12	Complex trajectory starting at (0, 0), with heading shown by arrows and desired trajectory by the dashed curve .	8